Texture Evolution During Hot Compression of CoCuFeMnNi Complex Concentrated Alloy Using Neutron Diffraction and Crystal Plasticity Simulations

Reshma Sonkusare[1,2] · Krishanu Biswas[1] · Weimin Gan[3] · H. G. Brokmeier[4] · N. P. Gurao[1]

Abstract CoCuFeMnNi complex concentrated alloy was subjected to hot compression at different temperatures and strain rates. Texture evolution for four representative samples was studied using electron backscatter diffraction, neutron diffraction and viscoplastic self-consistent simulations. EBSD revealed highest low angle grain boundaries and high angle grain boundaries for sample C (1273 K, 1 s^{-1}) indicating deformation and recrystallization, respectively, and highest very low angle grain boundaries for sample D (1273 K, 0.001 s^{-1}) indicating recovery. The bulk texture shows < 110 > compression texture, with dominance of partial slip over octahedral slip. Zener–Hollomon parameter was found to increase in the order D < B < C < A, with sample A (1073 K, 1 s^{-1}) exhibiting lowest crystallite size and sample D (1273 K, 0.001 s^{-1}) with highest crystallite size, consistent with the microstructural data. The texture analysis shows a partial slip-dominated dynamically recovered microstructure for sample A (1073 K, 1 s^{-1}) and discontinuous dynamically recrystallized microstructure for sample D (1273 K, 0.001 s^{-1}).

Keywords Complex concentrated alloys · High-temperature deformation · Processing maps · Neutron diffraction · Texture · VPSC

✉ Reshma Sonkusare
reshma28992@gmail.com

[1] Department of Materials Science and Engineering, Indian Institute of Technology, Kanpur, India

[2] Institute of Applied Materials, Karlsruhe Institute of Technology, Karlsruhe, Germany

[3] Institute of Materials Physics, Helmholtz-Zentrum Hereon, Geesthacht, Germany

[4] Institute of Materials Science and Engineering, TU Clausthal, Clausthal-Zellerfeld, Germany

1 Introduction

Controlling microstructure and texture during alloy processing is of paramount importance as it directly affects the properties and applications [1–4]. Texture can be regarded as an essential parameter for a complete microstructural characterization of a polycrystalline material as it provides information about anisotropic physical and technological properties and thermo-mechanical history like phase transition, plastic deformation, recrystallization, etc. The optimum processing conditions and operative micro-mechanisms during the deformation should be known as a material for large-scale production [5, 6]. Texture and microstructure evolution for conventional materials are well documented. However, for complex concentrated alloys (CCA), this data is limited.

Neutron diffraction is a standard and efficient bulk texture measurement technique for polycrystalline materials [7, 8]. Neutrons interact weakly with the matter and hence have high penetration depth; 10^2–10^3 times more than laboratory X-rays [9]. The sample size for neutron diffraction can be up to cm^3 for bulk texture and it provides data with high quality and much higher accuracy than X-rays measurement. Moreover, neutron scattering length and scattering angle 2Θ are independent of each other, unlike X-ray diffraction technique.

Wu et al. [10] reported that evolution of lattice strains and texture in single phase FCC FeCoNiCrMn complex concentrated alloy (CCA) during tensile test, obtained using neutron diffraction, was similar to that in conventional FCC metals and alloys, and operation of mixed dislocations was found to be the operative deformation mechanism in the alloy. Wang et al. [11] studied deformation behaviour of FeCoCrNi CCA at room temperature and cryogenic temperature, using neutron diffraction and observed that with decrease in temperature, the stacking fault energy declined.

This led to increase in twin formation, which increased the strength and ductility of the alloy at 77 K. Cai et al. [12] investigated deformation mechanisms in hot extruded and annealed single phase FCC $FeCoCrNiMo_{0.23}$ CCA, using combination of neutron diffraction and electron microscopy. It was observed that Mo addition contributed to solute solution strengthening and thereby increased the strength of the alloy. The as-extruded CCA had low stacking fault energy (~ 19 mJ/m^2) and had microstructure with twins and microbands, which led to high strength and ductility. Whereas, the annealed sample had high strength due to presence of Mo-rich intermetallic particles, formed because of decomposition of the alloy. Fu et al. [13] investigated the deformation mechanisms during tensile deformation of $Fe_{50}Mn_{30}Co_{10}Cr_{10}$ transformation induced plasticity (TRIP) CCA, using in situ neutron diffraction. Multiple stages were observed during the deformation. Elastic deformation was the first stage, followed by FCC to HCP transformation at the yield point (~ 200 MPa) and then stage two was TRIP in addition to dislocation slip. In stage three, twins started to nucleate in HCP phase (at 400 MPa load). At last, stage four included combination of compression twins, multiple twin systems in addition to slip and TRIP.

The authors have studied the processing map of CoCuFeMnNi CCA and their processing–microstructure–mechanical property co-relationship [14–17], but the texture evolution has not been discussed. The alloy has face-centered cubic (FCC) grains with FCC copper-rich nanoclusters inside the grains as well as at the grain boundaries. In the present investigation, four representative samples at extreme temperature and strain rates were selected to study the texture evolution, using electron backscatter diffraction (EBSD), neutron diffraction and viscoplastic self-consistent (VPSC) simulations, to understand the fundamental microstructural development of the alloy during hot compression. The extreme temperature and strain rate values are based on the processing map of the CoCuFeMnNi CCA, studied earlier by the authors [8].

2 Materials and Methods

2.1 Experimental Details

Equiatomic CoCuFeMnNi alloy was prepared using induction melting. Small cylindrical samples (15 mm height, 10 mm diameter) were subjected to isothermal hot compression test upto 50% reduction in Gleeble 3800 thermo-mechanical simulator, after homogenization treatment at 1273 K for 24 h (Fig. 1a). The details are provided elsewhere [8]. The deformation was performed in two-phase region as obtained from CALPHAD [10]. Four samples at

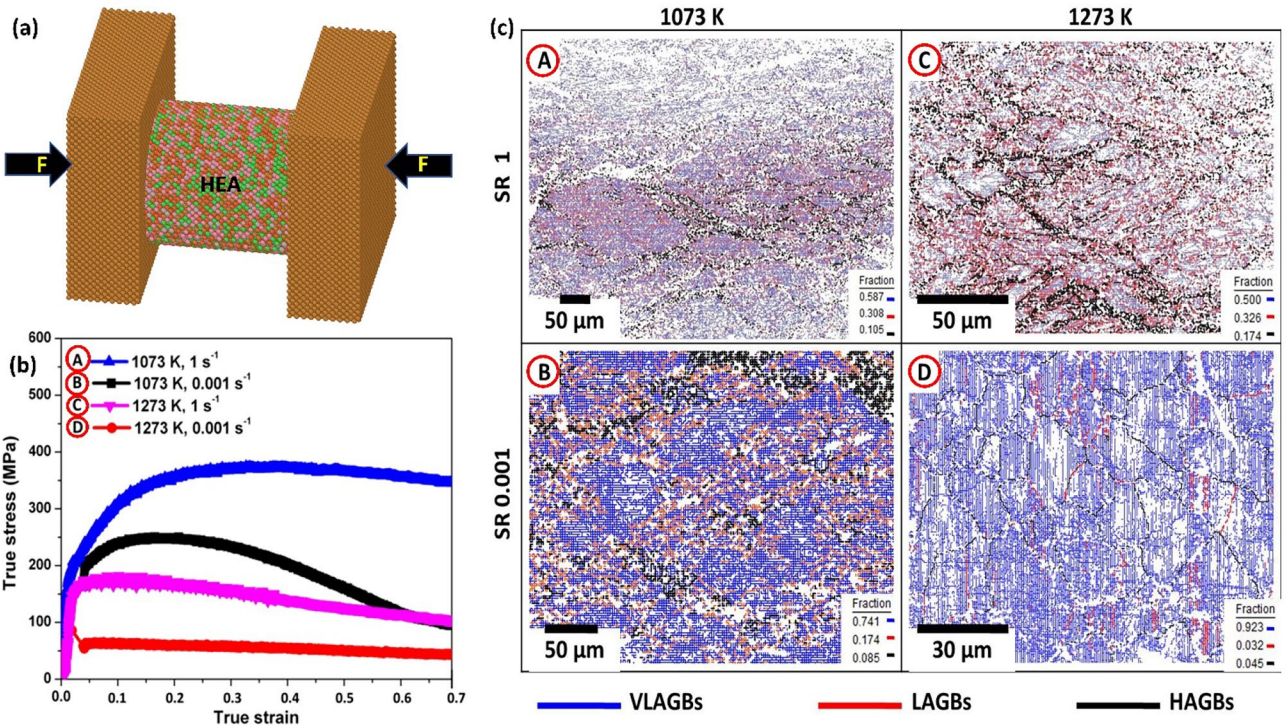

Fig. 1 **a** Compression schematic in Gleeble thermo-mechanical simulator, **b** True stress–strain curves, **c** Grain boundary map of the hot deformed CoCuFeMnNi complex concentrated alloy at extreme temperature and strain rate (corresponding encircled curve shown in (**b**))

extreme temperature (1073 K, 1273 K) and strain rate (1 s^{-1}, 0.001 s^{-1}) range have been used in the present investigation, with the nomenclature as given in Table 1.

Microstructural investigation was carried out using field emission–scanning electron microscope (FE-SEM) equipped with electron backscatter diffraction (EBSD) detector. The samples were prepared metallographically [8], by polishing with emery paper and alumina cloth followed by colloidal silica polishing. EBSD scans were acquired with a step size of 0.2 µm. The data was analyzed using TSL-OIM software.

Bulk texture measurement was carried out using the neutron diffractometer STRESS-SPEC (FRM-II, Garching, Germany). An incident monochromatic neutron beam with a wavelength of 0.142 nm and Ge monochromator crystal was used for the analysis. The measurement was done in transmission mode with a slit size of 2 cm diameter and the diffracted neutrons were detected by an area detector. Vanadium was used as a standard material. Staubli RX160 robot was used for texture measurement as well as for changing the sample. STeCa (stress and texture calculator) software was used to convert the raw data to pole figures by fitting the Braggs peak by Gaussian function. Complete orientation distribution function was determined from the pole figures using Resmat software. The texture of the deformed samples was depicted using inverse pole figures along the compression axis. Due to the deformation history, a rotational texture symmetry was obtained, and one inverse pole figure in compression direction represented the quantitative texture best.

2.2 Simulation Details

Viscoplastic self-consistent (VPSC) simulations [18–20] were utilized to simulate the texture of the hot compressed samples. The strain rate within the grain is given by the following equation.

$$\varepsilon_{ij} = \gamma^0 \sum_s m_{ij}^s \left(\frac{m_{kl}^s \sigma_{kl}}{\tau_0^s} \right)^n \tag{1}$$

where γ^0 = normalizing strain rate, s = slip system, m^s = symmetric Schmid tensor associated with slip system (s), n = rate sensitivity inverse, τ^s = threshold value of stress, σ_{kl} and ε_{ij} are deviatoric stress and strain rate. The evolution of critical resolved shear stress (CRSS) for slip or twinning with respect to strain is controlled by the Voce law as follows:

$$\tau(\Gamma) = \tau_0 + \left(\tau_1 + \theta_1 \Gamma\right)\left[1 - \exp\left(\frac{-\theta_0 \Gamma}{\tau_1}\right)\right] \tag{2}$$

where Γ = total accumulated shear strain on all the activated slip systems. The four parameters τ_0, τ_1, θ_0 and θ_1 represents initial CRSS, back-extrapolated CRSS, initial hardening rate and the asymptotic hardening rate, respectively. The values of Voce hardening parameters used in the simulation are given in Table 2. The following velocity gradient (L, s^{-1}) has been employed for the VPSC simulation.

$$L = \begin{pmatrix} 0.5 & 0 & 0 \\ 0 & 0.5 & 0 \\ 0 & 0 & -1 \end{pmatrix} \tag{3}$$

500 grains with random texture were generated and compression was carried out using n-effective model, with octahedral slip and partial slip mode. The simulations were carried out for two values of inverse strain rate sensitivity (2 and 20), and temperature of 1273 K was considered. The texture obtained from VPSC was plotted using Resmat software in the form of inverse pole figures (IPF).

3 Results and Discussion

Figure 1b shows the true stress–strain curves of the four samples at extreme temperature (1073 and 1273 K) and strain rate range (1 and 0.001 s^{-1}). The flow stress decreases with increase in temperature but increases with increase in strain rate. The flow softening in the stress–strain curves is due to restoration mechanisms like dynamic recovery (DRV) and dynamic recrystallization (DRX). Dynamic recrystallization leads to flow softening whereas, dynamic recovery leads to steady state behaviour in the stress–strain curves.

Table 2 Voce hardening parameters used for the VPSC simulations

Slip system	τ_0	τ_1	θ_0	θ_1
Octahedral slip {111}<1 $\bar{1}$ 0>	1	0.6	0.3	0.1
Partial slip {111}<11 $\bar{2}$>	0.95	0.6	0.3	0.1

Table 1 Nomenclature for the hot compressed samples of CoCuFeMnNi alloy and their grain boundary character distribution (GBCD) from EBSD

Nomenclature	Temperature (K)	Strain rate (s^{-1})	Grain boundary character distribution		
			VLAGB fraction	LAGB fraction	HAGB fraction
A	1073	1	0.587	0.308	0.105
B	1073	0.001	0.741	0.174	0.085
C	1273	1	0.500	0.326	0.174
D	1273	0.001	0.923	0.032	0.045

Earlier investigation on CoCuFeMnNi CCA shows phase separation between Cu-rich and Cu-lean phases, with Cu-rich phase at the grain boundaries. Figure 1c shows the grain boundary maps of the four samples. The blue, red and black colour lines indicate very low angle grain boundaries (VLAGBs) (2°–5°), low angle grain boundaries (LAGBs) (5°–15°) and high angle grain boundaries (HAGBs) (15°–65°), respectively. The grain boundary maps show significant differences in the microstructure of the four samples. All the images show more HAGBs at the grain boundaries which consist of Cu-rich phase, whereas grains are Cu-lean phase. Sample A (1073 K, 1 s^{-1}) shows the highest peak stress in the stress–strain curve. Sample B (1073 K, 0.001 s^{-1}) has the second highest peak stress and highest fraction of LAGBs and HAGBs (Table 1), indicating deformation and recrystallization, respectively. However, sample D (1273 K, 0.001 s^{-1}) has the highest fraction of VLAGBs, indicating dynamic recovery. It shows recrystallization and grain growth for both the phases and hence has lowest peak stress in the stress–strain curve.

Bulk texture measurement of the four samples was carried out using neutron diffraction technique. It was difficult to differentiate between the peaks of Cu-rich and Cu-lean phase with FCC structure in the neutron diffraction, and therefore, the alloy was treated as a single phase. Figure 2a shows the neutron diffraction profile, where the two orange arcs indicate (111) and (200) peaks of the FCC alloy. These two peaks were used to determine the inverse pole figures for the hot compressed samples as shown in Fig. 2b. Three samples (A, B, C) show $<110>$ type of texture, which is generally observed for compression of FCC materials. Whereas, for sample D (1273 K, 0.001 s^{-1}), $<001>$ type of texture is observed. $<001>$ is the recrystallization texture for compression of FCC materials and it is evident from the microstructure that all the parent grains are replaced by recrystallized new grains and hence $<001>$ texture is observed.

Line profile analysis (LPA) was carried out from neutron diffraction data, to investigate the microstructural parameters of the hot compressed samples. Microstructural parameters include average crystallite size, micro-strain within the crystallites and average dislocation density of the two phases present in the alloy (Table 3). The following equations have been utilized for calculation of the three parameters [21, 22].

$$B\cos\theta_B = \frac{K\lambda}{D} + 4\varepsilon\sin\theta_B \tag{4}$$

$$\rho = \frac{2\sqrt{3}\varepsilon}{Db} \tag{5}$$

where B = peak broadening ($B = \sqrt{B^2_{sample} - B^2_{instrument}}$), θ_B = Bragg angle, λ = wavelength (0.012 nm in this case), K = constant, D = crystallite size, ε = micro-strain, b = Burgers vector and ρ = dislocation density. Sample A shows highest dislocation density and lowest crystallite size, leading to highest peak stress in the true stress–strain curve. Whereas, sample D exhibits the lowest dislocation density and the highest crystallite size, due to presence of recrystallized grains with grain growth, also evident from the microstructure. The volume fraction of $<110>$ fiber texture component, calculated from the neutron diffraction data, is highest in all the four cases.

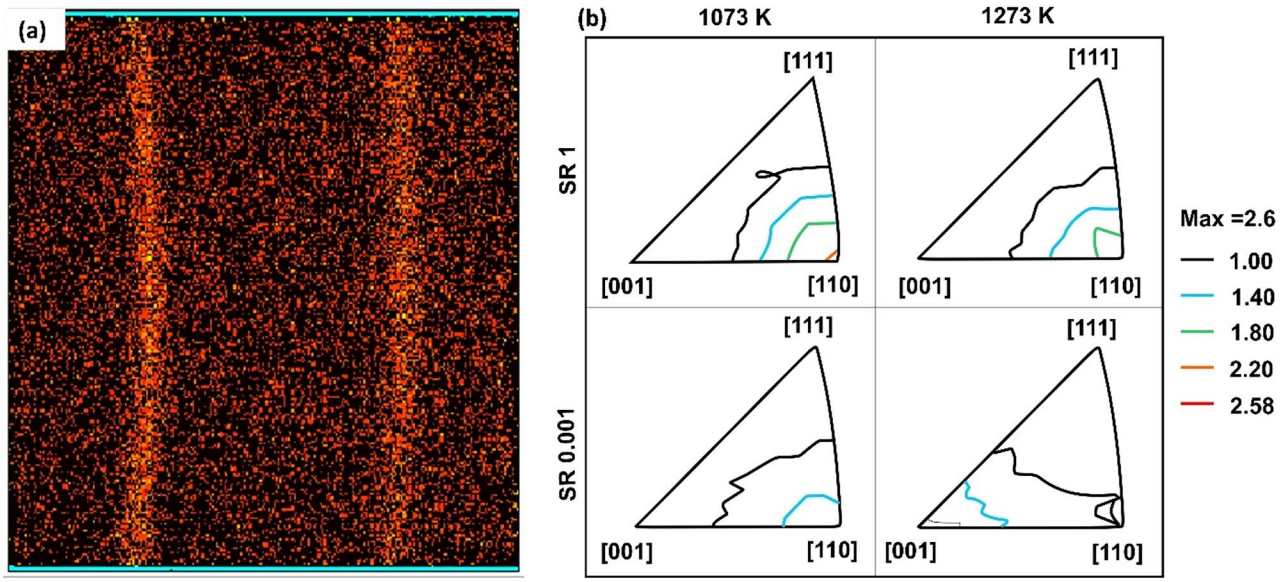

Fig. 2 **a** Neutron diffraction 2D images, **b** Inverse pole figures of hot compressed CoCuFeMnNi complex concentrated alloy

Table 3 Line profile analysis from neutron diffraction data

Sample nomenclature	Sample conditions	Crystallite size (nm)	Micro-strain (%)	Dislocation density (m^{-2})	Volume fraction of fibre texture components		
					100	101	111
A	1073 K, 1 s^{-1}	100	0.872	11.9×10^{13}	17.99	18.99	8.11
B	1073 K, 0.001 s^{-1}	110	0.855	10.6×10^{13}	9.10	30.70	8.82
C	1273 K, 1 s^{-1}	110	0.856	10.6×10^{13}	10.25	25.74	11.23
D	1273 K, 0.001 s^{-1}	130	0.678	7.1×10^{13}	6.62	34.22	8.12

The combined effect of strain rate ($\dot{\varepsilon}$) and temperature (T) can be studied by a parameter called Zener-Hollomon parameter [23], which can be described by the following equation.

$$Z = \dot{\varepsilon} \exp\left(\frac{Q}{RT}\right) \tag{6}$$

where Q = activation energy for deformation (394 kJ/mol in the present case [8]) and R = universal gas constant. Li et al. [24] described the relation of Z with microstructural and mechanical properties like yield strength (YS), peak stress, ultimate tensile strength (UTS), grain size, dislocation density, etc. Z is directly proportional to strength, defect density and microstrain and inversely proportional to grain size. In the present case, Z increases in the order D < B < C < A. It can be clearly observed that sample A has highest Z, highest peak stress, lowest crystallite size and highest dislocation density. However, sample D has lowest Z, lowest peak stress, highest crystallite size and lowest dislocation density.

VPSC simulations were carried out for an in-depth understanding of deformation micro-mechanisms. Since twins are not observed in the microstructure, only octahedral ($\{111\}<1\,\bar{1}\,0>$) and partial ($\{111\}<11\,\bar{2}>$) slip modes have been considered during simulation. The simulated IPF shows <110> type of texture for both the cases (Fig. 3a, c)

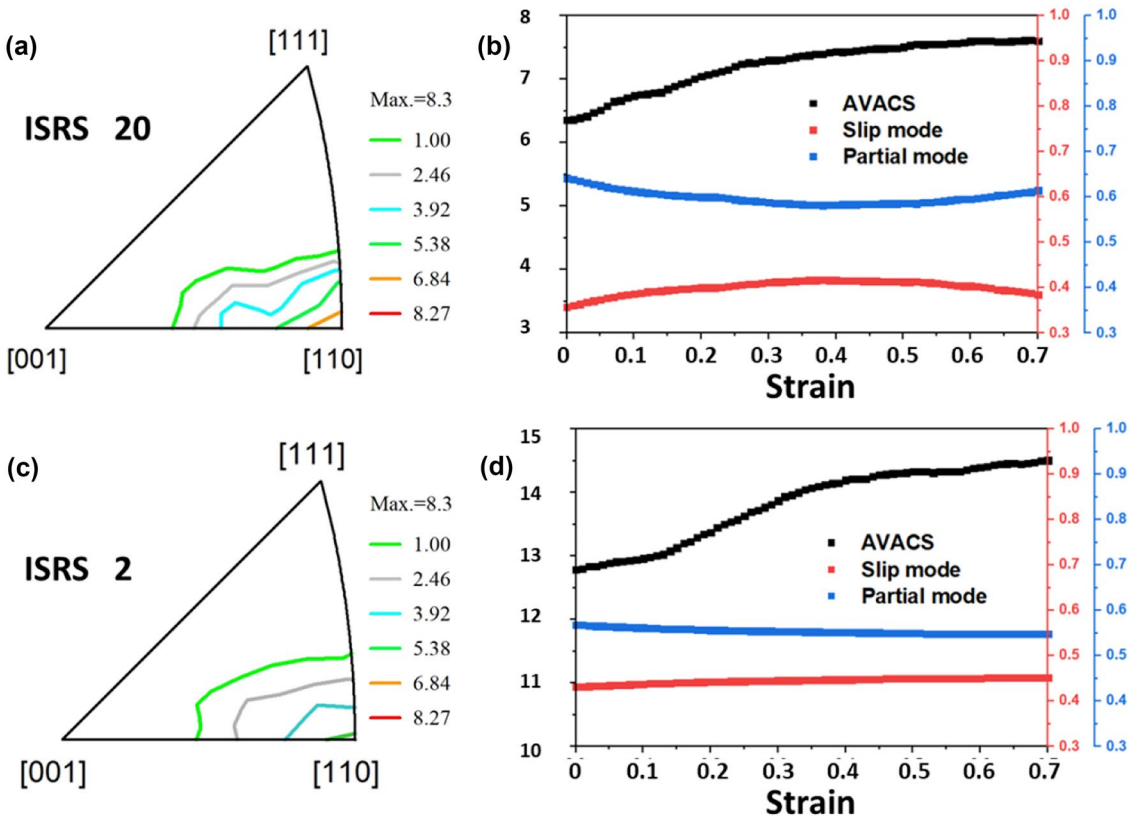

Fig. 3 VPSC Simulation: Inverse pole figure **a** ISRS = 20, **c** ISRS = 2, average active slip systems and activity of slip mode (mode 1) and partial mode (mode 2) for **b** ISRS = 20, **d** ISRS = 2

which is characteristic of compression of FCC materials. It can be observed that texture is strong at high inverse strain rate sensitivity (ISRS) (=20) and weak at ISRS (=2), indicating that texture can be modified using the ISRS parameter. The activity plot for octahedral and partial slip indicates that partial slip is more dominant than octahedral slip at all values of true strain. It also indicates that the average active slip system increases as a function of strain and number of average active slip systems are more when ISRS is low (=2). Since VPSC cannot account for DRX, therefore DRX texture was not modelled.

4 Conclusions

In the present work, texture evolution of the hot compressed samples of CoCuFeMnNi CCA has been studied using neutron diffraction with crystal plasticity simulations. The major conclusion from this study is as follows.

(1) Microstructural investigation using EBSD revealed highest fraction of LAGBs and HAGBs for sample compressed at 1073 K and 0.001 s^{-1} (sample B), indicating deformation and dynamic recrystallization, respectively and highest fraction of VLAGBs for sample compressed at 1273 K and 0.001 s^{-1} (sample D), indicating dynamic recovery.

(2) Line profile analysis indicated lowest dislocation density and highest crystallite size for sample compressed at 1273 K and 0.001 s^{-1} (sample D), due to completely recrystallized grains of both the phases and hence, lowest peak stress value among the four samples. Sample compressed at 1073 K and 1 s^{-1} (sample A) exhibited highest dislocation density and lowest crystallite size, leading to highest peak stress. The value of Zener–Hollomon parameter increased in the order D < B < C < A.

(3) Macro-texture obtained using neutron diffraction and VPSC simulations was <110> type, which was the characteristic FCC compression texture, except for sample compressed at 1273 K and 0.001 s^{-1} (sample D) where <001> FCC recrystallization texture was observed. VPSC revealed dominance of partial slip over octahedral slip even at high-temperature deformation.

Acknowledgements The authors acknowledge Texture Laboratory (ACMS, IIT Kanpur) and Neutron Diffraction facility (FRM-II, Garching, Germany). RS would like to acknowledge Dr. Nirmal Kumar for his help in improving the manuscript.

References

1. Sarkar A, Roy S, and Suwas S, *Mater Charact* **62** (2011) 35. https://doi.org/10.1016/j.matchar.2010.10.007
2. Roy S, and Suwas S, *J Alloys Compd* **548** (2013) 110, https://doi.org/10.1016/j.jallcom.2012.08.123
3. Aranas C M, Shen Y J, Rodrigues S F, and Jonas J J, *Metall Mater Trans A* **47** (2016) 4357, https://doi.org/10.1007/s11661-016-3655-8
4. Jonas J J, Poliak E I, and Najafizadeh A, *Mater Sci Forum* **539** (2007) 100, https://doi.org/10.4028/www.scientific.net/MSF.539-543.100
5. Samal S, Rahul M R, Kottada R S, and Phanikumar G, *Mater Sci Eng A* **664** (2016) 227, https://doi.org/10.1016/j.msea.2016.04.006
6. Rahul M R, Samal S, Venugopal S, and Phanikumar G, *J Alloys Compd* **749** (2018) 1115, https://doi.org/10.1016/j.jallcom.2018.03.262
7. Brokmeier H G, *Phys B: Condens Matter* **234–236** (1997) 977, https://doi.org/10.1016/S0921-4526(96)01230-6
8. Sahu V K, Sonkusare R, Biswas K, and Gurao N P, *J Indian Inst Sci* (2022).
9. Brokmeier H G, Gan W M, Randau C, Voller M, Rebelo-Kornmeier J, and Hofmann M, *Nucl Instrum Methods Phys Res Sect A: Accel, Spectrom, Detect Assoc Equip* **642** (2011) 87, https://doi.org/10.1016/j.nima.2011.04.008
10. Wu Y, Liu W H, Wang X L, Ma D, Stoica A D, Nieh T G, He Z B, and Lu Z P, *Appl Phys Lett* **104** (2014) 051910. https://doi.org/10.1063/1.4863748
11. Wang Y, Liu B, Yan K, Wang M, Kabra S, Chiu Y-L, Dye D, Lee P D, Liu Y, and Cai B, *Acta Mater* **154** (2018) 79. https://doi.org/10.1016/j.actamat.2018.05.013
12. Cai B, Liu B, Kabra S, Wang Y, Yan K, Lee P D, Liu Y, *Acta Mat* **127** (2017) 471. https://doi.org/10.1016/j.actamat.2017.01.034
13. Fu S, Bei H, Chen Y, Liu T K, Yu D, and An K, *Mater Res Lett* **6** (2018) 620. https://doi.org/10.1080/21663831.2018.1523239
14. Sonkusare R, Swain A, Rahul M R, Samal S, Gurao N P, Biswas K, Singh S, and Nayan N, *Mater Sci Eng A* **759** (2019) 415, https://doi.org/10.1016/j.msea.2019.04.096
15. Prasad Y, Rao K, and Sasidhar S, *Hot Working Guide: A Compendium of Processing Maps, second edition*, ASM international, Ohio, (2015).
16. Sonkusare R, Janani D, Gurao N P, Sarkar S, Sen S, Pradeep K G, and Biswas K, *Mater Chem Phys* **210** (2018) 269, https://doi.org/10.1016/j.matchemphys.2017.08.051
17. Agarwal R, Sonkusare R, Jha S R, Gurao N P, Biswas K, and Nayan N, *Mater Des* **157** (2018) 539, https://doi.org/10.1016/j.matdes.2018.07.046
18. Lebensohn R, and Tomé C, *Acta Metall* **41** (1993) 2611, https://doi.org/10.1016/0956-7151(93)90130-K
19. Toth L S, Estrin Y, Lapovok R, and Gu C, *Acta Mater* **58** (2010) 1782, https://doi.org/10.1016/j.actamat.2009.11.020
20. Sonkusare R, Biswas K, Al-Hamdany N, Brokeier H G, Kalsar R, Schell N, and Gurao N P, *Mater Sci Eng A* **782** (2020) 139187, https://doi.org/10.1016/j.msea.2020.139187
21. Heczel A, Kawasaki M, Labar J, Jang J, Langdon T G, and Gubicza J, *J Alloys Compd* **711** (2017) 143, https://doi.org/10.1016/j.jallcom.2017.03.352
22. Ganji R S, Karthik P S, Rao K B S, and Rajulapati K V, *Acta Mater* **125** (2017) 58, https://doi.org/10.1016/j.actamat.2016.11.046
23. Dieter G, *Mechanical metallurgy, SI Metric edition*, McGraw-Hill Book Company, Singapore (1988).
24. Li Y S, Zhang Y, Tao N R, and Lu K, *Acta Mater* **57** (2009) 761, https://doi.org/10.1016/j.actamat.2008.10.021